J Magn Reson Imaging. Author manuscript; available in PMC 2022 May 01.

Retrospective distortion and motion correction for free-breathing DW-MRI of the kidneys using dual echo EPI and slice-to-volume registration

Jaume Coll-Font, Ph.D.[1,2], **Onur Afacan, Ph.D.**[2,3], **Scott Hoge, Ph.D.**[2,4], **Harsha Garg, M.D.**[3], **Kumar Shashi, M.D.**[3], **Bahram Marami, Ph.D.**[5], **Ali Gholipour, Ph.D.**[2,3], **Jeanne Chow, M.D.**[2,3], **Simon Warfield, Ph.D.**[2,3], **Sila Kurugol, Ph.D.**[2,3]

[1]Cardiology, Massachusetts General Hospital, Boston, MA, United States

[2]Harvard Medical School, Boston, MA, United States

[3]Radiology, Boston Children's Hospital, Boston, MA, United States

[4]Radiology, Brigham and Women's Hospital, Boston, MA, United States

[5]Icahn School of Medicine at Mount Sinai, New York, NY, United States

Abstract

BACKGROUND—Diffusion-weighted MRI (DW-MRI) of the kidneys is a technique that provides information about microstructure of renal tissue without requiring exogenous contrasts such as Gadolinium, and it can be used for diagnosis in cases of renal disease and assessing response-to-therapy. However, physiological motion and large geometric distortions due to main B_0 field inhomogeneities degrade the image quality, reduce the accuracy of quantitative imaging markers and impede their subsequent clinical applicability.

PURPOSE—To retrospectively correct for geometric distortion for free-breathing DW-MRI of the kidneys at 3T, in the presence of non-static distortion field due to breathing and bulk motion.

STUDY TYPE—Prospective.

SUBJECTS—10 Healthy volunteers (ages 29-38, 4 females)

FIELD STRENGTH/SEQUENCE—3T; DW-MR dual-echo EPI sequence (10 b-values and 17 directions) and a T_2 volume.

ASSESSMENT—The distortion correction was evaluated subjectively (Likert scale 0-5) and numerically with the cross-correlation between the diffusion weighted images at b=0 s/mm2 and a T2 volume. The intravoxel incoherent motion (IVIM) and diffusion tensor (DTI) model fitting performance was evaluated using their root-mean-squared error (nRMSE) and the coefficient of variation (CV%) of their parameters.

STATISTICAL TESTS—Statistical comparisons were done using Wilcoxon tests.

Corresponding Author Info: Jaume Coll-Font, 360 Longwood ave. 5th floor, 02115, Boston (MA), USA. (857) 218-5172, jcoll-font@mgh.harvard.edu.

RESULTS—The proposed method improved the Likert scores by 1.1+/−0.8 ($p<0.05$), the cross-correlation with the T_2 reference image by 0.13+/−0.05 ($p<0.05$) and reduced the nRMSE by 0.13+/−0.03 ($p<0.05$) and 0.23+/−0.06 ($p<0.05$) for IVIM and DTI, respectively. The CV% of the IVIM parameters (slow and fast diffusion, and diffusion fraction for IVIM and mean diffusivity and fractional anisotropy for DTI) was reduced by 2.26+/−3.98% ($p= 6.971\times10^{-2}$), 11.24+/−26.26% ($p= 6.971 \times10^{-2}$), 4.12+/−12.91% ($p=0.101$), 3.22+/−0.55% ($p<0.05$) and 2.42+/−1.15% ($p<0.05$).

DATA CONCLUSION—The results indicate that the proposed Di+MoCo method can effectively correct for time varying geometric distortions and for misalignments due to breathing motion. Consequently, the image quality and precision of the DW-MRI model parameters improved.

Keywords

Diffusion weighted imaging (DWI); distortion compensation; motion compensation; free-breathing; kidney imaging

INTRODUCTION

Diffusion-weighted MRI (DW-MRI) of kidneys has been increasingly used to evaluate renal disease and will be potentially useful in pediatric populations because it is free of any exogenous contrast agent such as Gadolinium and ionizing radiation, eliminating the associated risks (1–5). DW-MR images are usually acquired at multiple b-values and directions and quantitative parameters are estimated by fitting a signal decay model such as an apparent diffusion coefficient (ADC) model, diffusion tensor (DTI) model or intravoxel incoherent motion (IVIM) model among others (6–8). The parameters of these models provide markers of change in the microstructure of the renal tissue for both the cortex and medulla and can be used for diagnosis in cases of renal disease and assessing response-to-therapy (9–12). However, physiological motion (such as respiration, bowel motility) and large geometric distortions due to inhomogeneities in the main B_0 field during Echo Planar Imaging (EPI) acquisitions degrade the image quality, reduce the accuracy of quantitative imaging markers and impede the clinical applicability of the technique (13, 14).

B_0 field inhomogeneities result in large geometric distortions due to the long EPI readout times (14). Even though geometric distortions are not specific to imaging of the kidneys, these sources of error are particularly challenging to correct in abdominal imaging mainly due to two factors: 1) there are sharp changes in susceptibility close to the tissue of interest (e.g. pockets of air in the bowel, stomach and lungs); 2) the local field inhomogeneities are affected by motion (e.g. respiration, bowel motility and bulk motion when patient moves) and change across images acquired at different positions of the organs. Moreover, since physicians prefer to acquire the images of the kidneys along the oblique coronal orientation, it is not possible to reduce the field of view, and, in consequence, the number of k-space lines to reduce the effects of distortion (15).

Distortion in DW-MR images is often corrected retrospectively by estimating the distortion field after registering a single pair of images acquired with opposite phase encoding direction and, hence, have opposite distortion effects (16),(17). This approach then uses the estimated field from the image pair to correct for distortion in the rest of DW-MR images. However, an essential assumption of this approach is that there is no motion throughout the scan and the B_0 field inhomogeneities are constant over time (18, 19). This assumption does not hold when there is motion. In the case of abdominal DW-MR imaging the motion can be produced by unavoidable physiological motion of the organs such as the kidneys, bulk motion of the subject (children) and motility of the bowel. In order to compensate for geometric distortion in the presence of motion, a method was recently proposed for DW-MRI of the brain. In this work, the method was extended and evaluated for application to geometric distortion correction in abdominal DW-MRI (21, 22).

Another challenge in DW-MRI of the kidneys is the misalignment of volumes due to motion, which is challenging to correct due to the 3D nature of motion and different motion patterns of left and right kidneys (4, 15). Currently used 2D registration methods are limited due to out of plane motion. Moreover, the differences in contrast observed across DW-MR images acquired at different diffusion weightings (e.g. the low signal in images acquired at high b-values), which introduces further ill-posedness into the motion correction. To overcome this problem, a model-based 3D registration approach for abdominal DW-MR imaging was previously proposed by Kurugol et al. (24, 25). This approach registers each volume to a template volume generated from the signal decay model at the same b-value, and therefore have the same contrast. Here we use similar idea of registering each slice to a 3D template volume generated from the previous b-value.

This paper presents a method for distortion correction in the presence of motion and a method for motion compensation using a 3D slice to volume registration technique for free-breathing DW-MR imaging of the kidneys at 3T.

METHODS

Distortion Correction in the Presence of Motion

A novel dual-echo sequence has been implemented to acquire two EPI readouts with opposite phase encoding directions for each slice and diffusion weighting. The two EPI readouts are introduced to estimate distortion field at each position and therefore account for the change in distortion field due to motion, e.g. when organs are placed at different locations (21, 22, 27). Due to short time between the first and second readout (~30-50 msec), the motion of the kidneys between these two images is negligible. Consequently, these images are affected by the same distortion field and distortion can be corrected for each pair. The sequence is composed of a standard echo and EPI readout followed by a second echo that reverses the phase encoding in the second EPI readout. The resulting two images have opposite phase encodings and maintain the same DW encoding and distortion field. Despite negligible difference between distortion fields between the two echoes, the time between images is sufficient for T_2 attenuation to be considerable in some tissues within the field of view. As seen in the example acquisitions of Figure 1, there are notable variations in signal intensity in the muscle and liver tissues between the first and second echo images (middle-left and left columns respectively) and a corresponding reduction in SNR, which make further pre-processing necessary. To that objective, histogram equalization and a median filter steps are applied to the first and second echo images to balance the signal intensity between them and to improve SNR. Afterwards, TOPUP is applied to estimate the distortion field of each image pair. The resulting field is finally used to correct for the distortion of the original images (before histogram normalization) and the sum-of-squares of the two images is calculated to generate a single distortion-corrected DW-MR image.

Slice to Volume Registration for Motion Correction

The motion between slices is corrected using a 3D slice to volume registration algorithm, which registers a static 3D volume to each slice, at similar b-values. The registration parameters for consecutively acquired slices are regularized with a dynamic model of motion. This model assumes that the motion of each kidney is rigid, changes smoothly over time and, in consequence, the rigid motion parameters can be regularized with a Kalman filter (28). Hence, the rigid transformation parameters for each slice $z_k = [\theta_x, \theta_y, \theta_z, t_x, t_y, t_z]$ –where 'k' is the slice number, and θ and t are rotation and translation parameters in the x, y, z coordinates– can be characterized by the function $z_k = z_{k-1} + v_k$, where v_k is a random variable drawn from a 0-mean Gaussian distribution $(v_k \sim \mathcal{N}(0, S_k))$. At each iteration, the algorithm registers the 3D template volume to each slice using rigid registration with the mutual information metric –implemented in ITK (29)– and then filters the registration parameters $\{z_k\}_{k=1}^{K}$ with the Kalman filter. The estimated transformations are then applied to each slice to obtain a point cloud of the data points positioned at their correct anatomical locations. Finally, to go back to a regular 3D grid from the point cloud, the intensity values of each voxel in the 3D volume are interpolated with a weighted average of the points in the cloud within a spherical neighborhood around each voxel, and weighted with a Gaussian kernel applied to the distances between the voxel of interest and the points in the neighborhood.

Full Pipeline

The overall processing pipeline to do distortion (Di) and motion compensation (MoCo) consists of the steps described in algorithm 1.

Algorithm 1: Di+MoCo Pipeline

- Image acquisition with dual-echo sequence
- Crop images to the desired FOV
- Di step:
    - Apply histogram normalization to each image
    - Apply median filter to improve SNR
    - Estimate distortion field given each pair of histogram normalized images from dual echo acquisition
    - Apply the estimated distortion field to the original images
    - Generate DW images with sum-of-squares of every distortion corrected pair

- MoCo step:
    - Crop a rectangular region of interest for each organ in each slice (e.g. each kidney)
    - Until maximum iterations do:
        - Generate an average 3D volume template using registered slices at previous b-value
        - 3D Slice-to-volume registration: Register 3D template volume to each slice in the next b-value image.
        - Smooth estimated rigid registration parameters with Kalman filter
        - Apply inverse of estimated transform to each slice and interpolate the voxel intensities to the original grid after registration
- Fit DW-MRI signal decay model to the motion and distortion corrected data

EXPERIMENTS

The data was acquired after obtaining consent with the appropriate IRB approval. DW-MR images were acquired from 10 healthy subjects (ages 29-38, 4 females) in oblique coronal orientation along the kidneys. The subjects were imaged with a dual-echo EPI sequence and acquired 168 DW-MR volumes (10 b-values and 17 directions) on a 3T Siemens Prisma scanner with echo times (TE1/TE2) 72ms/108ms, repetition time (TR) 2600ms, 18 coronal slices, pixel bandwidth (BW) 1775Hz/pixel, matrix size 128x128, voxel size 2.81x2.81x4 mm, b-values 0, 10, 30, 50, 80,120, 200, 400, 600 and 800 s/mm^2). The two EPI readouts in the dual-echo sequence were acquired with phase encodings along the right-left (R->L) and left->right (L->R) directions. A T_2 Half-Fourier Single Shot Turbo Spin Echo (T_2-HASTE) volume was acquired as reference using the same FOV as the diffusion sequence. Its parameters were (TE/TR) 96ms/1600ms, (BW) 710Hz/pixel, matrix size 320x288 and voxel size 1.125x1.125 mm.

After reconstructing each pair of R->L/L->R dual-echo DW images, the distortion correction step was applied to estimate the distortion field. Every pair of distortion corrected R->L/L->R images was then combined with sum-of-squares and the collection of 168 DW images for the study was compiled.

Afterwards, each kidney was cropped separately and the consecutively acquired slices were registered with the slice-to-volume registration as described in the methods section. Finally, a spatially regularized IVIM and DTI models were fitted to the DW-MRI volumes using a fusion bootstrap moves algorithm and a weighted least squares method, respectively (30). In order to avoid the effects of fast diffusion due to microcapillary perfusion in the DTI model, its fitting was restricted to the volumes with b-value range of $b \geq 200$ s/mm^2. To provide estimates of the estimation uncertainty, a permutation bootstrap technique was applied. It randomly selected the images encoded along 15 gradient directions and 12 non-directional b=0 images from the DW-MR data and fitted the diffusion models to those subsets of images.

Evaluation:

The DW images were first evaluated qualitatively by three radiologists. Each radiologist was independently shown a DW image at b=0 with and without distortion correction alongside the corresponding T2-HASTE image as reference. The radiologists were asked to evaluate the image quality for each kidney using a 5-point Likert scale corresponding to 1-Completely distorted, 2-Mostly distorted, 3-Neutral, 4-Mostly undistorted and 5-Undistorted. The larger the score, the better the image quality.

The improvement in geometry of the DW image with the distortion correction step was then evaluated quantitatively by computing the correlation of all R->L DW-MR volumes at b=0 s/mm2, before and after distortion correction against the reference T2-HASTE image. Specifically, the normalized cross-correlation (NCC) between the DW-MR image and T_2-HASTE reference, resampled to the image space of the DW-MR images, was computed following the formulation defined in equation (1). Given two input images (x,y) with means $\bar{x}, \bar{y}$ and standard deviations $\sigma_x \sigma_y$, NCC was given by

$$NCC = \frac{1}{\sigma_x \sigma_y} \frac{1}{N} \sum_{i,j} (x_i - \bar{x})^T (y_i - \bar{y})$$

Afterwards, the improvement in diffusion model fit using both IVIM and DTI was quantified. We report on the goodness of fit as the normalized root-mean-squared error (nRMSE) between the original data and the model prediction, as well as the precision, measured by the coefficient of variation (CV) of the model parameters: the diffusivity (D), perfusion (D*) and perfusion fraction (f) for IVIM and the mean diffusivity (MD) and fractional anisotropy (FA) for DTI. For each comparison, Wilcoxon tests were computed and statistical significance was determined for $p<0.05$.

To evaluate the specific improvements in the previously described metrics provided by each step, the distortion and motion correction (Di+MoCo) results were compared against alternative combinations of the steps in the processing pipeline. All metrics were computed on the data without any processing (no correction), processing limited to the distortion correction (Di) as well as to slice-to-volume registration of the acquired data (MoCo).

Software implementation and data processing:

All DW images were reconstructed with in-house software developed in MATLAB. Distortion and motion compensation were done automatically with a pipeline implemented in python. The pipeline included the distortion correction step using TOPUP (C++) available in https://fsl.fmrib.ox.ac.uk/fsl/fslwiki/FslInstallation), an in-house implementation of the slice-to-volume registration (C++) and the model fitting. The latter was done using in-house software for the IVIM fit with spatial regularization (C++) and the open-source software in DIPY for DTI (30, 31). The analysis of the results was done in python and the statistical tests performed with the Wilcoxon test implementation in the SCIPY package (https://www.scipy.org/).

Two sets of masks were generated to analyze the data. The first set, shown in Figure 2, was done using the b=0 s/mm^2 images before and after distortion correction and was used to compute the statistics in NCC, nRMSE and CV of the results. The second consisted of the delineation of the cortex and medulla for each subject and was used to compute the parameters reported in Table 1. These were generated using B_0 maps as well as the FA and MD parameter maps computed from the DWI-MR data. The masks used for analysis were generated with ITK-SNAP. Masks were segmented by JCF once and reviewed by SK afterwards. JCF and SK have 2 and 5 years of experience in MR imaging of the kidneys, respectively.

RESULTS

Figures 1 and 2 compare the reference T_2-HASTE image against the original R->L, L->R images, and the distortion corrected R->L image. Figure 1 shows the T_2-HASTE compared to the acquired DW-MR images and their combination after distortion correction. Figure 2 shows the T_2-HASTE image with the contours of the kidneys segmented using the R->L, L->R and distortion corrected DW-MR images. The original R->L and L->R images present large geometric distortions in the direction of the phase encoding (left to right) that warp the kidneys, particularly the upper half, near the lungs, and the edges close to the bowel. On the other hand, the kidneys in the distortion corrected images are better aligned with the reference T_2 image and their distortion is reduced. The results of evaluation by three radiologists showed that, the distortion corrected DW-MR images resulted in increased subjective Likert scores compared to the non-distortion corrected images, indicating improved quality for each subject. The average Likert score of image quality was increased from 2.6+/−1.0 to 3.7+/−1.0 ($p<0.05$) after distortion. The NCC results for each subject are reported in Figure 3. The distortion corrected images aligned significantly better and had significantly higher correlation with the T_2 HASTE reference image (NCC=0.53±0.08) compared to the DW-MRI images without distortion correction (NCC= 0.40±0.10) ($p<0.05$).

We illustrate the motion of the kidneys over the 168 DW-MR images in Figure 4a. Since each DW-MR image was acquired sequentially, the plot shows the motion of the kidneys over time. A line of voxels (indicated by the red line in the left panel) was plotted across all DW-MR images before and after motion correction. Before correction, the kidneys showed oscillatory motion due to breathing while, after motion compensation the oscillations were reduced, and the kidneys were better aligned over the entire sequence. The registration parameters estimated for this subject, shown in Figure 4b, present a similar oscillatory pattern, which is more pronounced in translation along the vertical (z) direction. Numerically, motion compensation improved the NCC with the T_2-HASTE reference image. The motion-compensated DW-MR volumes without distortion correction increased the NCC by 0.04 ($p<0.05$) and those with distortion correction further increased the NCC by 0.1 ($p<0.05$). The volumes with both distortion and motion compensation had the highest NCC.

Figure 5 compares the parameter maps estimated from the distortion and motion corrected data against the data without any correction for a representative subject. From left to right, each column shows the IVIM parameters --diffusivity, perfusion and perfusion fraction -- and the parameters of the DTI model -- mean diffusivity and fractional anisotropy. The maps obtained from the “no correction” data present a large number of outliers in the diffusion and perfusion parameters and the medulla and cortex structures are not well defined. In contrast, after Di+MoCo, the structures of the kidney, medulla and cortex can be differentiated, particularly in the f and FA maps. The estimated parameters for both IVIM and DTI model on the medulla and cortex regions are summarized in Table 1. These results were generated by using the cortex and medulla masks shown in Figure 6.

To illustrate the behavior of the data over b-value, Figure 6 also shows the signal intensity of two voxels (one on the cortex and another on the medulla) before and after applying the Di+MoCo processing. The original signal presents large variability, which is reduced after applying Di+MoCo. Before correction, the values in the cortex present two distinct decays, one with fast decay that is consistent with the background voxels and another with slower decay, consistent with the cortex. On the other hand, the signal on the medulla does not present a multi-modal behavior, although before correction it is more consistent with the values observed in the cortex with Di+MoCo.

The goodness of fit for both the DTI and IVIM models was improved after applying the proposed Di+MoCo technique (Table 2). On average, the IVIM and DTI residuals were reduced by 0.13+/−0.03 ($p<0.05$) and 0.23+/−0.06 ($p<0.05$) over the original data (no correction). However, as seen in Figures 7 and 8, the reduction in nRMSE introduced by the MoCo step was larger compared to just applying the distortion correction step and there was no significant difference between MoCo and the joint Di+MoCo in the residuals of the IVIM fit ($p=0.439$), although the residual difference was significant for the DTI fit ($p<0.05$). Similarly, as reported in Table 2, the coefficient of variation decreased for all parameters although the reduction was statistically significant only for the DTI parameters. The differences in coefficient of variation between the original data (no correction) and the Di+MoCo data were 2.26+/−3.98% for the diffusivity ($p<0.05$), 11.24+/−26.26% for the perfusion ($p<0.05$), 4.12+/−12.91% for the fraction ($p=0.101$), 3.22+/−0.55% for the mean diffusivity ($p<0.05$) and 2.42+/−1.15% for the fractional anisotropy ($p<0.05$).

DISCUSSION

The results indicate that the proposed Di+MoCo DW-MRI technique, combining a dual-echo EPI acquisition with the steps for distortion and motion correction using the regularized slice-to-volume registration technique improve the precision of the estimated parameters of the diffusion models in both cortex and medulla compartments of the kidney. The dual echo acquisition enables correction of distortion when there is no motion between two echoes, which is followed by correction of motion between consecutively acquired slices.

Our method does not require breath-holds and allows for distortion and motion correction of kidney DW-MR images acquired during free-breathing and can therefore be used in uncooperative patients such as children. An alternative approach would be to acquire DW-

MR images with opposite phase encodings during breath-holds or with respiratory gating and estimate a static susceptibility-induced field (13). However, respiratory gating techniques increase the scan time >5 times, when compared to our free breathing dual-echo sequence according to previous reports (26). Moreover, respiratory gating cannot account for the irregular motion of the bowel, which introduces large distortion inconsistent with respiration (e.g. subject 2 in Figure 1). Incorporating simultaneous-multi-slice acquisition could further reduce the acquisition time-and would also improve the accuracy of the slice-to-volume registration as shown in previous work applied to brain imaging (26, 32).

Due to the change in contrast introduced by fast T_2 attenuation in the abdominal tissue, we needed to equalize the histograms of the opposing phase encoding images (i.e. Right (R) ->Left (L) and L->R images and we applied median filter to compensate for the loss in SNR. However, this step may be avoided in future work using an improved registration framework. Currently, we applied TOPUP, which uses the least-squares difference between the two images to align them and to correct for the effects of distortion. Incorporating alternative registration metrics such as mutual information, normalized cross correlation or metrics based on the DW models (33–35), might improve the reliability of the matches between the two images. Alternatively, the T_2 attenuation could be estimated and accounted for in the second echo images of the dual echo acquisition in order to correct for the change of intensity of the second echo images (36).

Here, we compensated for motion using a method that regularized over time with a Kalman filter. However, it would be possible to use alternative models, such as the discrete cosine transform to regularize over the registration parameters estimated for consecutively acquired DW-MRI slices (20). Further improvements to this method could include incorporating a diffusion signal decay model into the cost function, when registering the DW-MR images to the 3D template volume (20, 25).

The IVIM and DTI parameters estimated on the healthy volunteers agreed with those reported in the literature for healthy kidneys (5, 15). However, an advantage with respect to previous reports is that the parameter maps obtained are free of distortion and can be combined with those obtained with other sequences not affected by distortion (e.g. T_1 or T_2 maps).

The presented method could be beneficial for the standardization efforts in kidney DW imaging, as it addresses challenges that affect two major questions for which there is no current consensus (15, 37). First, with an effective distortion correction approach, the SNR benefits of 3.0 T imaging might outweigh the benefits of 1.5 T, and, second, free-breathing with motion compensation might be preferred over respiratory gating given the reduction of scan time offered when motion can be accurately compensated.

Limitations

The main limitation of the present study is the lack of a reference standard for the estimated DW-MRI model parameters beyond comparison to current literature. We therefore report the precision of the estimated parameters by computing the coefficient of variation. We report reduced coefficient of variation, indicating improved precision of the parameters with the proposed method. Similarly, another limitation of the current analysis is the choice of a single registration method for estimating the distortion field from dual echo images acquired with opposite phase encoding directions. Future work should compare the performance of alternative registration approaches to estimate the distortion field. (35, 38). Finally, this study is limited to only 10 healthy volunteers. Further work should include patient data to evaluate the benefits of this method in clinical practice.

Conclusion

We have presented a method for simultaneous geometric distortion (Di) and motion compensation (MoCo) for DW-MR imaging of the kidneys during free-breathing. Our results indicate that the proposed method can effectively correct for the B_0 field inhomogeneity related geometric distortions and the misalignments due to breathing motion. Consequently, the image quality and precision of the DW model parameters improved with the Di+MoCo DW-MRI technique.

Grant Support:

This work was supported partially by the Boston Children’s Hospital Translational Research Program Pilot Grant 2018, Society of Pediatric Radiology Multi-center Research Grant 2019, Crohn’s and Colitis Foundation of America’s (CCFA) Career Development Award, the AGA-Boston Scientific Technology Innovation Award 2018 and by NIDDK grant number R01 DK100404 and R21 DK123569 and NIBIB grant numbers R21 EB029627, R01 EB018988 and R01 EB019483 of the National Institutes of Health.

This work was supported partially by the Boston Children’s Hospital Translational Research Program Pilot Grant 2018, Society of Pediatric Radiology Multi-center Research Grant 2019, Crohn’s and Colitis Foundation of America’s (CCFA) Career Development Award, the AGA-Boston Scientific Technology Innovation Award 2018 and by NIDDK grant number R01 DK100404 and R21 DK123569 and NIBIB grant numbers R21 EB029627, R01 EB018988 and R01 EB019483 of the National Institutes of Health.

References

1. Vivier P-HH, Sallem A, Beurdeley M, et al.: MRI and suspected acute pyelonephritis in children: Comparison of diffusion-weighted imaging with gadolinium-enhanced T1-weighted imaging. Eur Radiol 2014; 24:19–25. [PubMed: 23884301]
2. Faletti R, Cassinis MC, Fonio P, et al.: Diffusion–Weighted Imaging and Apparent Diffusion Coefficient Values Versus Contrast–Enhanced MR Imaging in the Identification and Characterisation of Acute Pyelonephritis. Eur Radiol 2013; 23:3501–3508. [PubMed: 23887662]
3. Friedli I, Crowe LA, Berchtold L, et al.: New Magnetic Resonance Imaging Index for Renal Fibrosis Assessment: A Comparison between Diffusion-Weighted Imaging and T1 Mapping with Histological Validation. Sci Rep 2016; 6:1–15. [PubMed: 28442746]
4. van Baalen S, Leemans A, Dik P, Lilien MR, ten Haken B, Froeling M: Intravoxel incoherent motion modeling in the kidneys: Comparison of mono-, bi-, and triexponential fit. J Magn Reson Imaging 2017; 46:228–239. [PubMed: 27787931]
5. Bane O, Wagner M, Zhang JL, et al.: Assessment of renal function using intravoxel incoherent motion diffusion-weighted imaging and dynamic contrast-enhanced MRI. J Magn Reson Imaging 2016; 44:317–326. [PubMed: 26855407]
6. Le Bihan D, Breton E, Lallemand D, Aubin ML, Vignaud J, Laval-Jeantet M: Separation of diffusion and perfusion in intravoxel incoherent motion MR imaging. Radiology 1988; 168:497–505. [PubMed: 3393671]
7. Basser PJ, Mattiello J, Lebihan D: Estimation of the Effective Self-Diffusion Tensor from the NMR Spin Echo. J Magn Reson Ser B 1994; 103:247–254. [PubMed: 8019776]

8. Kurugol S, Freiman M, Afacan O, Perez-Rossello JM, Callahan MJ, Warfield SK: Spatially-constrained probability distribution model of incoherent motion (SPIM) for abdominal diffusion-weighted MRI. Med Image Anal 2016; 32:173–183. [PubMed: 27111049]
9. Düzenli K, Öztürk M, Yıldırım İO, Erdem G: The utility of diffusion-weighted imaging to assess acute renal parenchymal changes due to unilateral ureteral stone obstruction. Urolithiasis 2017; 45:401–405. [PubMed: 27709258]
10. Poynton CB, Lee MM, Li Y, et al.: Intravoxel incoherent motion analysis of renal allograft diffusion with clinical and histopathological correlation in pediatric kidney transplant patients: A preliminary cross-sectional observational study. Pediatr Transplant 2017; 21:1–8. [PubMed: 28474818]
11. Binser T, Phys D, Kessler TM: Noninvasive Assessment of Acute Ureteral Obstruction with A Prospective Study. Radiology 2009; 252:721–728. [PubMed: 19567650]
12. Thoeny HC, Binser T, Roth B, Kessler TM, Vermathen P: Noninvasive Assessment of Acute Ureteral Obstruction with Diffusion-weighted MR Imaging: A Prospective Study. Radiology 2009; 252:721–728. [PubMed: 19567650]
13. Borrelli P, Cavaliere C, Basso L, Soricelli A, Salvatore M, Aiello M: Diffusion Tensor Imaging of the Kidney: Design and Evaluation of a Reliable Processing Pipeline. Sci Rep 2019; 9:1–10. [PubMed: 30626917]
14. Jezzard P, Balaban RS: Correction for geometric distortion in echo planar images from B0 field variations. Magn Reson Med 1995; 34:65–73. [PubMed: 7674900]
15. Ljimani A, Caroli A, Laustsen C, et al.: Consensus-based technical recommendations for clinical translation of renal diffusion-weighted MRI. Magn Reson Mater Physics, Biol Med 2020; 33:177–195.
16. Chang H, Fitzpatrick JM: A Technique for Accurate Magnetic Resonance Imaging in the Presence of Field Inhomogeneities. IEEE Trans Med Imaging 1992; 11:319–329. [PubMed: 18222873]
17. Andersson JLR, Skare S, Ashburner J: How to correct susceptibility distortions in spin-echo echo-planar images: Application to diffusion tensor imaging. Neuroimage 2003; 20:870–888. [PubMed: 14568458]
18. Prohl AK, Scherrer B, Tomas-Fernandez X, et al.: Early white matter development is abnormal in tuberous sclerosis complex patients who develop autism spectrum disorder. J Neurodev Disord 2019; 11:36–52. [PubMed: 31838998]
19. Tax CM, Grussu F, Kaden E, et al.: Cross-scanner and cross-protocol diffusion MRI data harmonisation: A benchmark database and evaluation of algorithms. Neuroimage 2019; 195:285–299. [PubMed: 30716459]
20. Andersson JLR, Graham MS, Drobnjak I, Zhang H, Filippini N, Bastiani M: Towards a comprehensive framework for movement and distortion correction of diffusion MR images: Within volume movement. Neuroimage 2017; 152(February):450–466. [PubMed: 28284799]
21. Afacan O, Hoge WS, Wallace TE, Gholipour A, Kurugol S, Warfield SK: Dual-echo blip reversed EPI acquisition enables distortion correction in the presence of motion in diffusion-weighted MRI. In *Int Soc Magn Reson Med*. *Volume* 64; 2019:3–5.
22. Afacan O, Hoge WS, Wallace TE, Gholipour A, Kurugol S, Warfield SK: Simultaneous motion and distortion correction using dual- echo diffusion weighted MRI. J Neuroimaging 2020:1–5.
23. Kurugol S, Marami B, Afacan O, Warfield SK, Gholipour A: Motion-Robust Spatially Constrained Parameter Estimation in Renal Diffusion-Weighted MRI by 3D Motion Tracking and Correction of Sequential Slices. In Int Conf Med Image Comput Comput Interv. *Volume* 10555. Springer, Cham; 2017:75–85.
24. Kurugol S, Freiman M, Afacan O, et al.: Motion-robust parameter estimation in abdominal diffusion-weighted MRI by simultaneous image registration and model estimation. Med Image Anal 2017; 39:124–132. [PubMed: 28494271]
25. Kurugol S, Freiman M, Afacan O, et al.: Motion Compensated Abdominal Diffusion Weighted MRI by Simultaneous Image Registration and Model Estimation (SIR-ME). In Int Conf Med Image Comput Comput Interv. *Volume* 9351. NIH Public Access; 2015:501–509.
26. Tavakoli A, Krammer J, Attenberger UiI, et al.: Simultaneous Multislice Diffusion-Weighted Imaging of the Kidneys at 3 T. Invest Radiol 2020; 55:233–238. [PubMed: 31917764]

27. Gallichan D, Andersson JLR, Jenkinson M, Robson MD, Miller KL: Reducing distortions in diffusion-weighted echo planar imaging with a dual-echo blip-reversed sequence. Magn Reson Med 2010; 64:382–390. [PubMed: 20665782]
28. Marami B, Scherrer B, Afacan O, Erem B, Warfield SK, Gholipour A: Motion-Robust Diffusion-Weighted Brain MRI Reconstruction Through Slice-Level Registration-Based Motion Tracking. IEEE Trans Med Imaging 2016; 35:2258–2269. [PubMed: 27834639]
29. McCormick M, Liu X, Jomier J, Marion C, Ibanez L: ITK: enabling reproducible research and open science. Front Neuroinform 2014; 8(FEB):13–24. [PubMed: 24600387]
30. Freiman M, Perez-Rossello JM, Callahan MJ, et al.: Reliable estimation of incoherent motion parametric maps from diffusion-weighted MRI using fusion bootstrap moves. Med Image Anal 2013; 17:325–336. [PubMed: 23434293]
31. Garyfallidis E, Brett M, Amirbekian B, et al.: Dipy, a library for the analysis of diffusion MRI data. Front Neuroinform 2014; 8:8. [PubMed: 24600385]
32. Marami B, Scherrer B, Afacan O, Warfield SK, Gholipour A: Motion-Robust Reconstruction Based on Simultaneous Multi-slice Registration for Diffusion-Weighted MRI of Moving Subjects. In Int Conf Med Image Comput Comput Interv. Springer, Cham; 2016:544–552.
33. Kurugol S, Afacan O, Lee RS, et al.: Prospective pediatric study comparing glomerular filtration rate estimates based on motion-robust dynamic contrast-enhanced magnetic resonance imaging and serum creatinine (eGFR) to 99mTc DTPA. *Pediatr Radiol* 2020; 50:698–705.
34. Marami B, Scherrer B, Khan S, et al.: Motion-robust diffusion compartment imaging using simultaneous multi-slice acquisition. Magn Reson Med 2019; 81:3314–3329. [PubMed: 30443929]
35. Hedouin R, Commowick O, Bannier E, et al.: Block-Matching Distortion Correction of Echo-Planar Images with Opposite Phase Encoding Directions. IEEE Trans Med Imaging 2017; 36:1106–1115. [PubMed: 28092527]
36. Hilbert T, Schulz J, Marques JP, et al.: Fast model-based T2 mapping using SAR-reduced simultaneous multislice excitation. Magn Reson Med 2019; 82:2090–2103. [PubMed: 31273830]
37. Mendichovszky I, Pullens P, Dekkers I, et al.: Technical recommendations for clinical translation of renal MRI: a consensus project of the Cooperation in Science and Technology Action PARENCHIMA. Magn Reson Mater Physics, Biol Med 2019; 33:131–140.
38. Voss HU, Watts R, Uluğ AM, Ballon D: Fiber tracking in the cervical spine and inferior brain regions with reversed gradient diffusion tensor imaging. Magn Reson Imaging 2006; 24:231–239. [PubMed: 16563951]

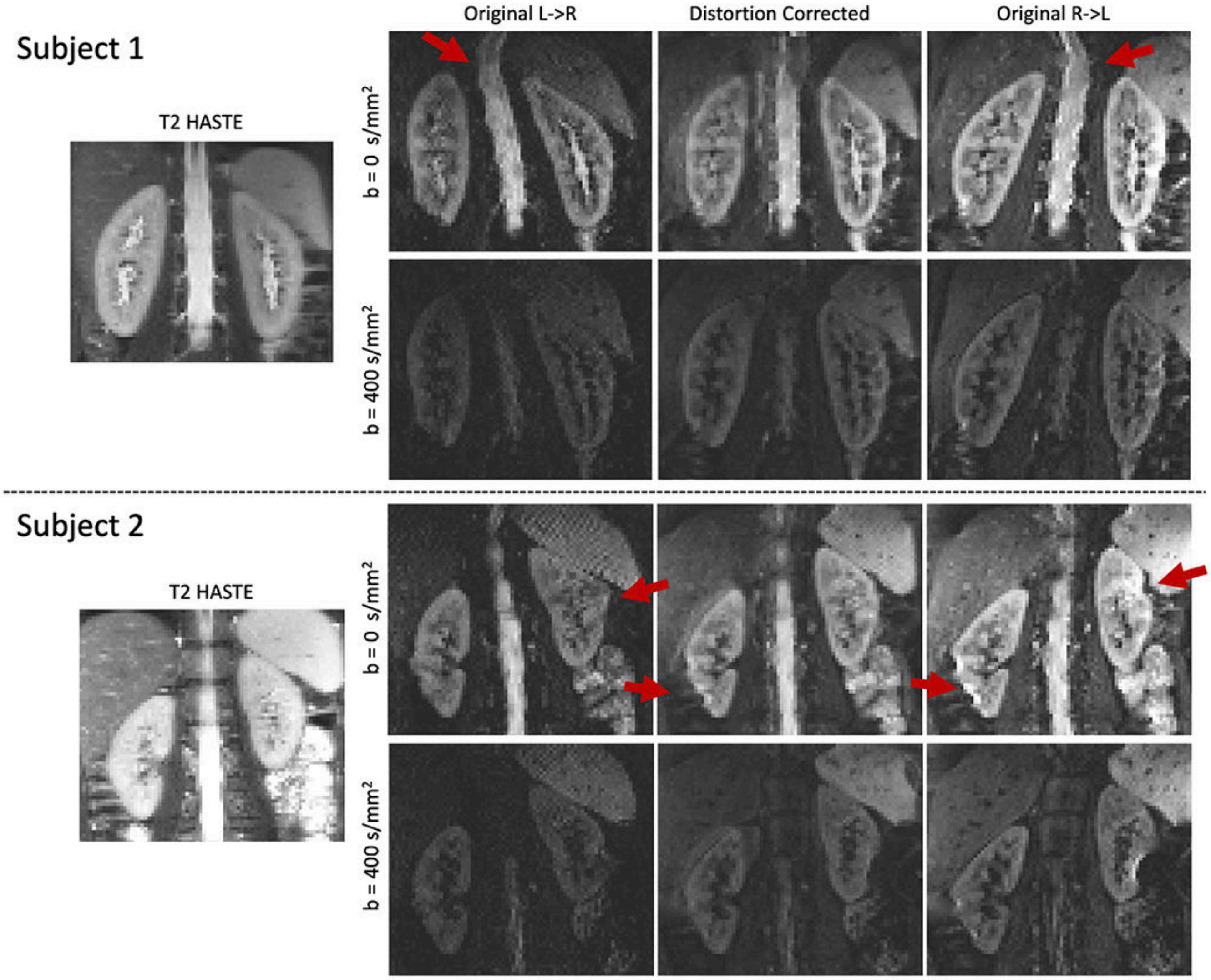

Figure 1.

The comparison of the reference T_2-HASTE image of two subjects and DW-MR images (for two b-values) before and after distortion correction for two representative subjects. The T_2-HASTE reference (left column), the original L->R image (middle left), original R->L image (right) and distortion corrected image (middle right) are shown. Red arrows indicate areas where distortion is present. The original images present large distortion, particularly in the upper part of the kidneys and near the bowel, indicated with red arrows. After distortion correction, the distortion is reduced in most of the kidney, although there are some remaining errors in the right kidney of subject 2 near the bowel, also indicated by the red arrows.

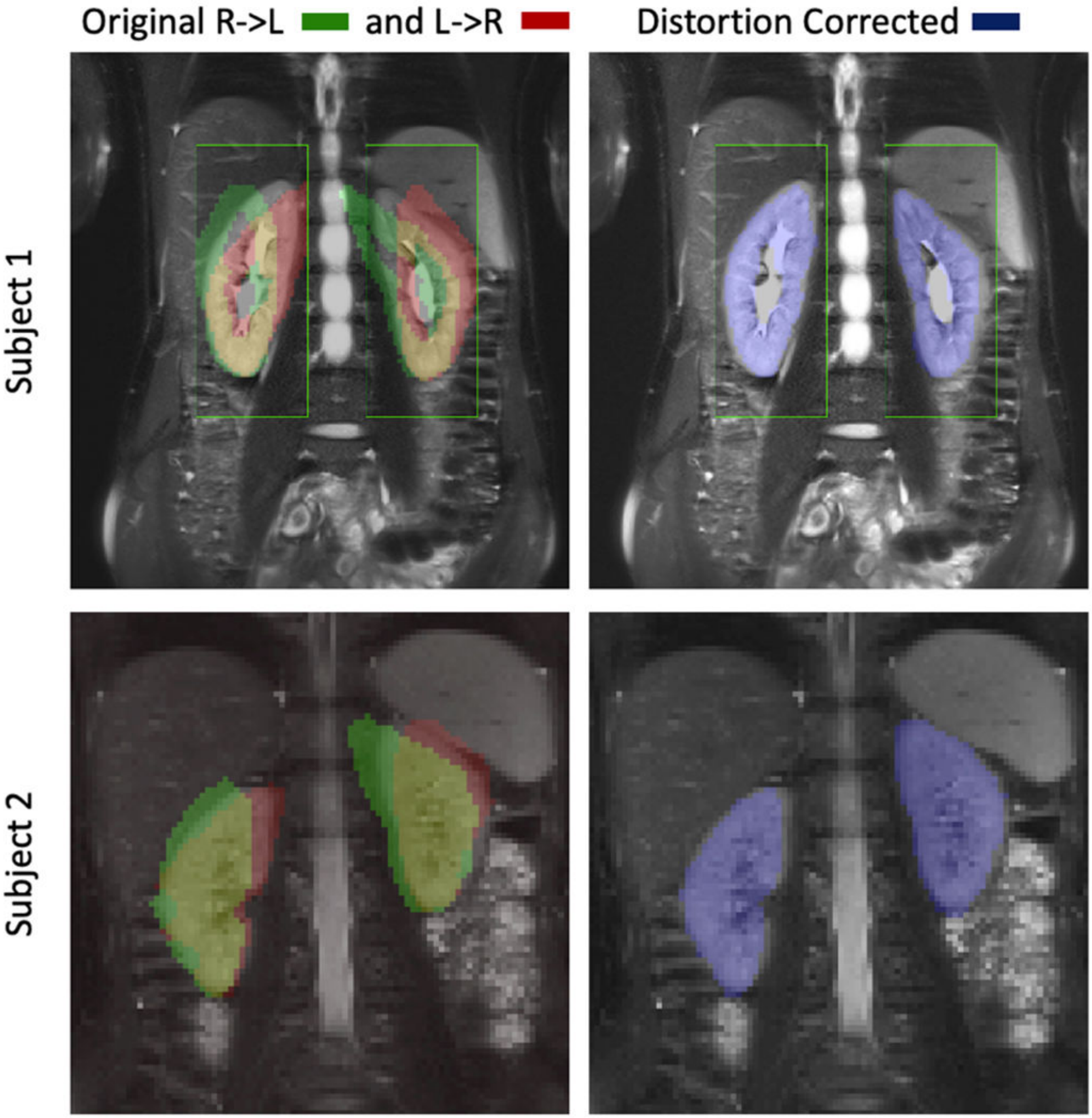

Figure 2.

Reference T_2-HASTE image and the segmented kidney masks from the DW images are shown for the L->R and R->L images without correction on the left and for the distortion corrected image on the right. Each row corresponds to one representative subject. The kidneys are severely distorted in the original DW images. After distortion correction, the kidneys are in good alignment with the reference image, which resulted in an increase in Likert score from 2.6+/−1.0 to 3.7+/−1.0 ($p<0.05$).

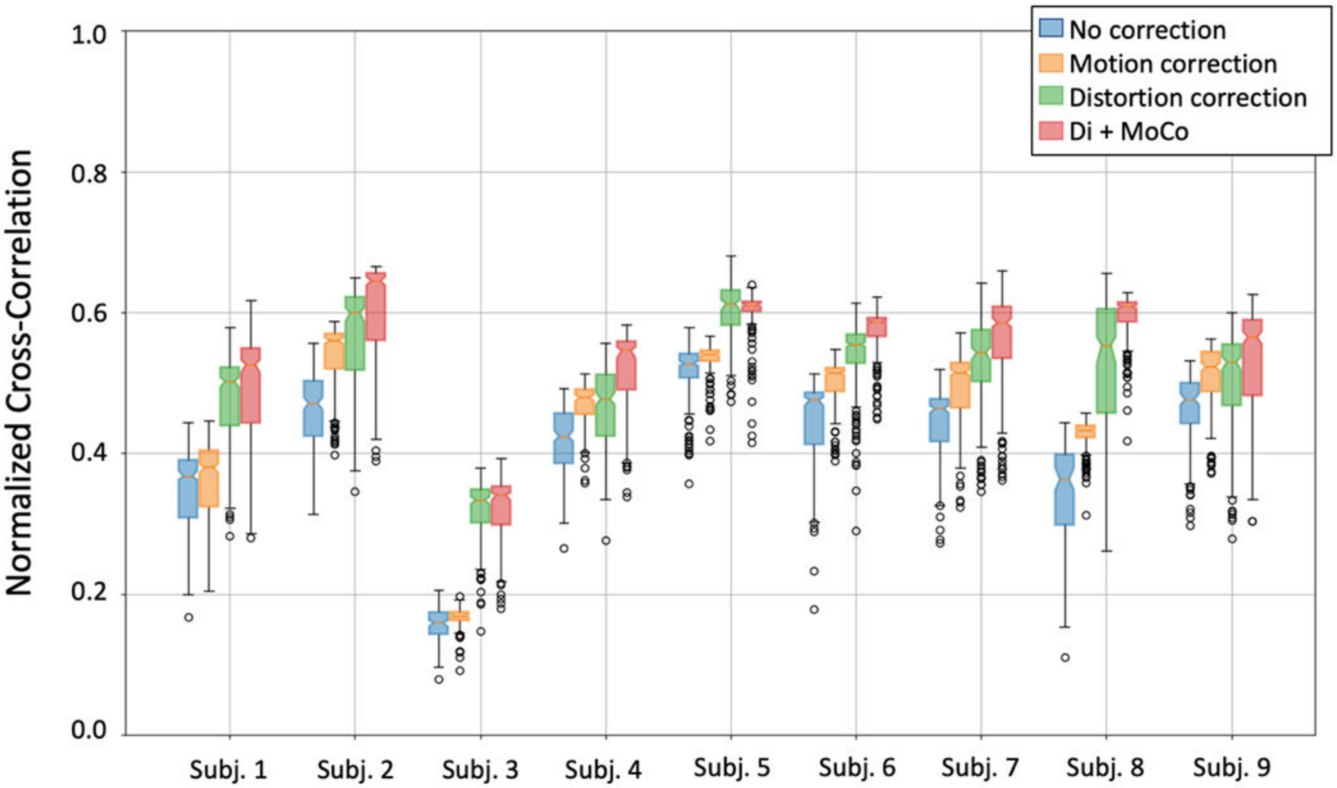

Figure 3.

Box plots of the normalized cross-correlation between the DW-MR and the T_2-HASTE volumes for 9 subjects. The box plots for each subject correspond to different processing approaches: no processing (green), motion correction only (orange), distortion correction only (green) and distortion plus motion correction (red). Distortion correction produces the largest increase in cross correlation, while motion compensation adds further improvements that are relatively smaller.

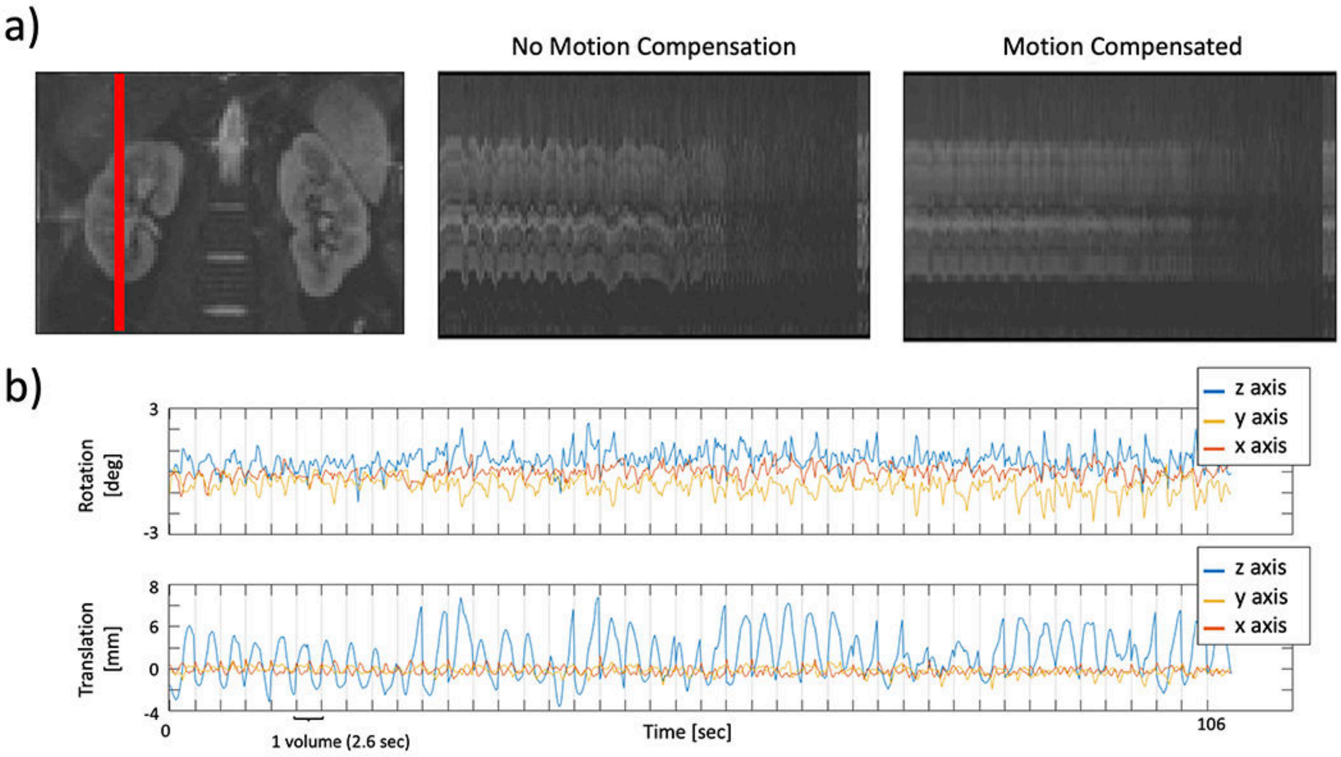

Figure 4.

Temporal evolution of a line of voxels from one kidney over different DW acquisitions and the registration parameters of the consecutively acquired slices during the first 1.8 min for a representative subject. The leftmost column in (a) shows the images of the cropped kidneys with a red line indicating the selected line of voxels plotted on the right. The middle panel shows the line plot for the volume with distortion correction, but no motion compensation and right panel shows the line plot for the Di+MoCo volume. Panel (b) shows the rotation and translation parameters (top and bottom). The time to acquire each volume (2.6 sec) is indicated with vertical lines.Before motion compensation, the line plot shows large oscillations due to breathing. On the other hand, motion compensation corrects those oscillations and aligns the DW-MR volumes in the acquired sequence.

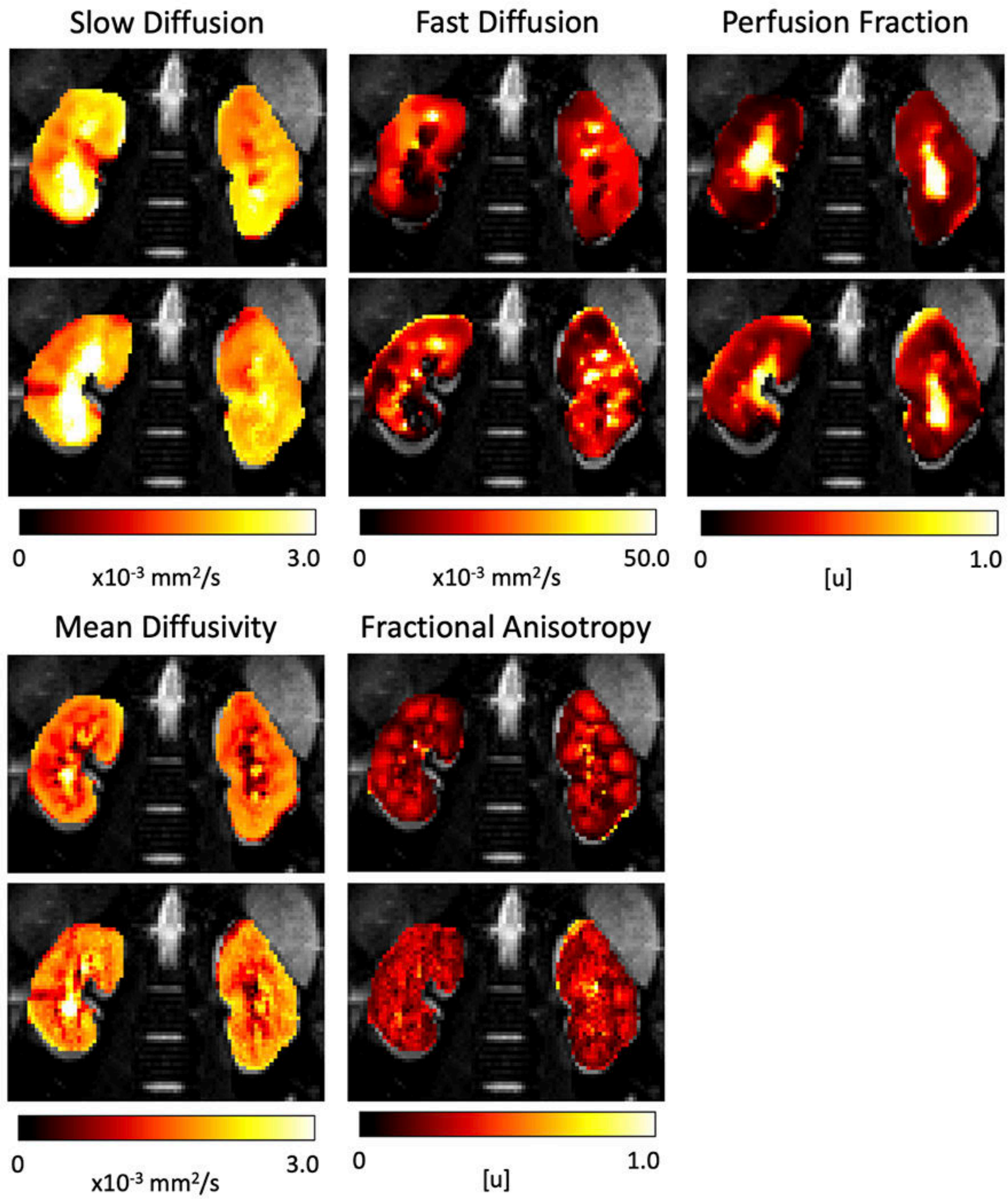

Figure 5.

IVIM and DTI parameters estimated on the original data without processing (no correction) and after distortion and motion compensation (Di+MoCo) for a representative subject. The columns correspond to the slow diffusion (D), fast diffusion (D*), perfusion fraction (f) of the IVIM model and the mean diffusivity (MD) and fractional anisotropy (FA) parameters of the DTI model. The parameter maps obtained after Di+MoCo processing have fewer outliers and discontinuities. Moreover, the medulla and cortex can be better identified in the perfusion fraction (f) and fractional anisotropy (FA) maps of Di+MoCo.

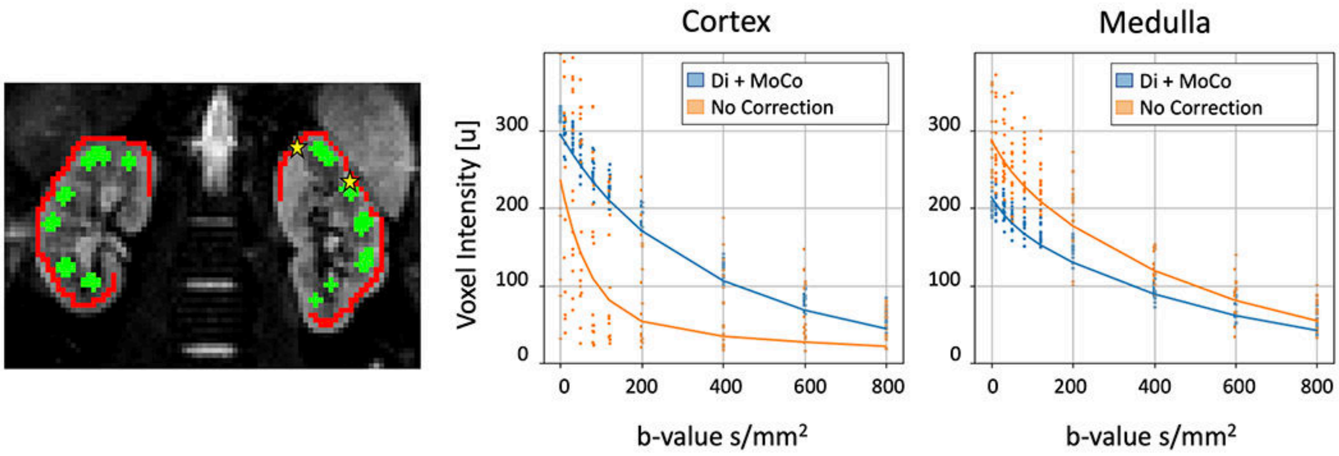

Figure 6.

Left image shows an example of the cortex and medulla masks (red and green) overlaid over a B_0 image. The middle and right panels show the IVIM fit to the data in one voxel of the cortex and medulla (indicated with the yellow stars) before corrections and after distortion and motion compensation. The dots correspond to the data in the voxel and the lines to the fitted IVIM model. Distortion and motion compensation reduce the variability of the voxel intensity over multiple acquisitions.

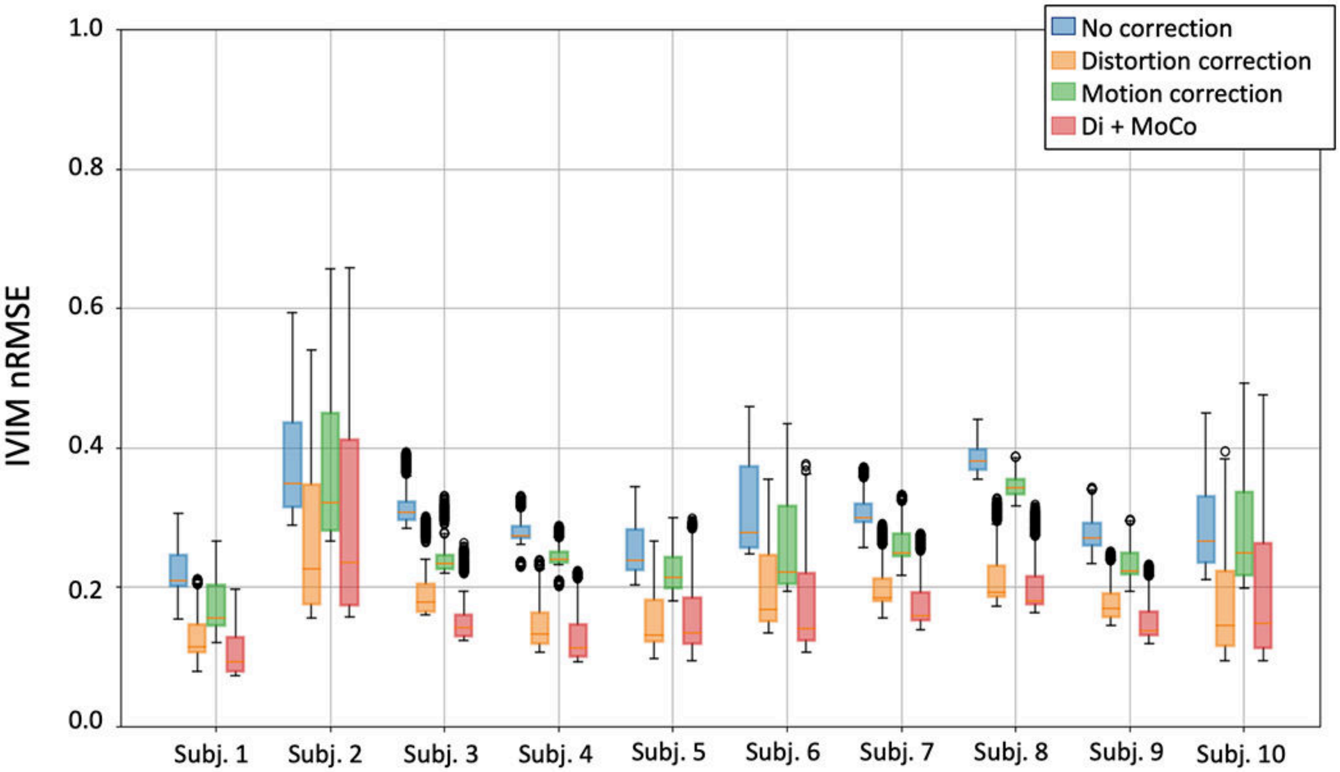

Figure 7.

IVIM goodness for every subject reported as nRMSE. The box plots for each subject correspond to different processing approaches: no processing (blue), distortion correction only (orange), motion correction only (green) and distortion plus motion correction (red). Motion compensation provides the highest improvement in IVIM model fit, while the improvement provided by distortion correction is relatively smaller.

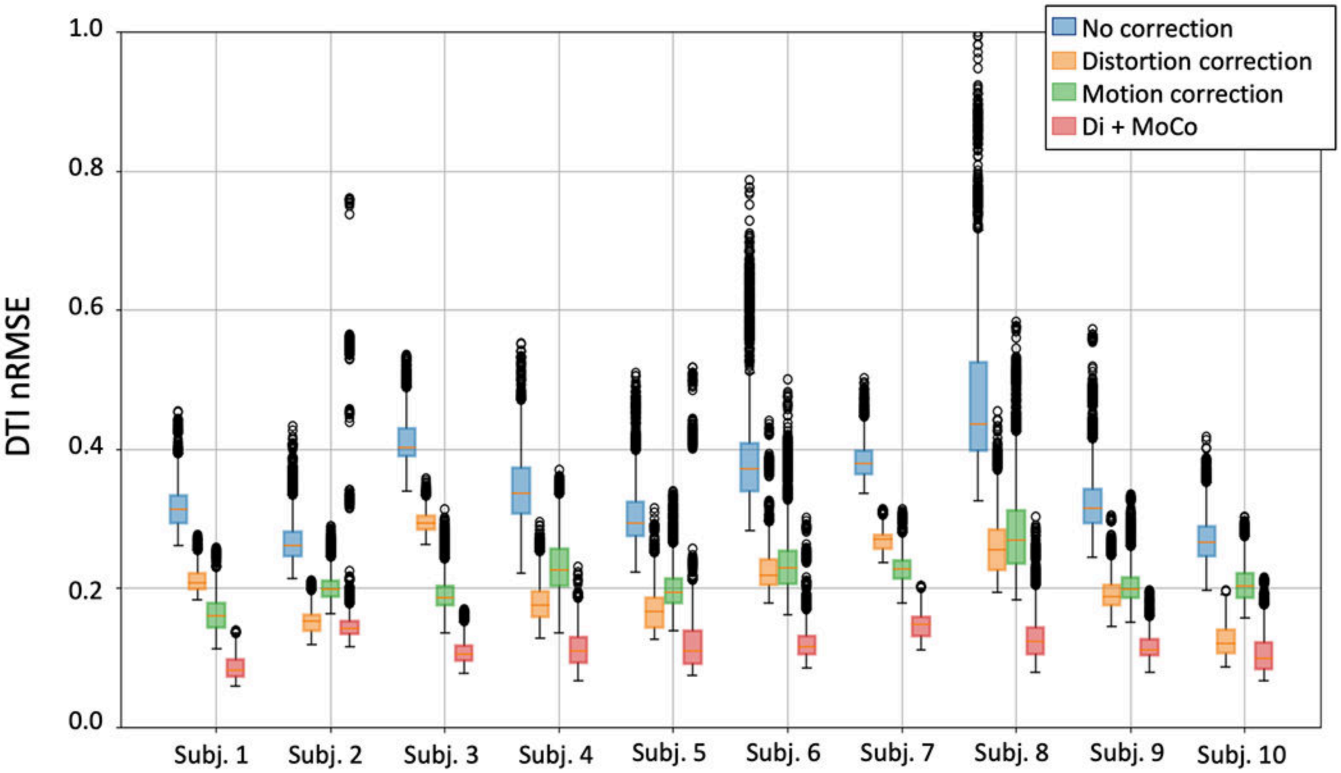

Figure 8.

DTI goodness for every subject reported as nRMSE. The box plots for each subject correspond to different processing approaches: no processing (blue), distortion correction only (orange), motion correction only (green) and distortion plus motion correction (red). Motion compensation provides the highest improvement in DTI model fit, while the improvement provided by distortion correction is small.

Table 1.

IVIM parameters estimated on the cortex and medulla for all subjects. The values were computed from manually segmented masks of the medulla and cortex of the kidneys. Both the IVIM and DTI parameters of the subjects are in concordance with the values reported in the literature for healthy subjects.

Param / Subject		**IVIM**			**DTI**	
		Slow diff. (D) [x103 mm2/s]	**Fast diff. (D*) [x103 mm2/s]**	**Perf. Frac, (f) [%]**	**Mean Diffusivity (MD) [x103 mm2/s]**	**Fractional Anisotropy (FA) [%]**
s1	**cortex**	1.7+/−0.12	17+/−7.76	17+/−3.18	1.6+/−0.36	13+/−5.22
	medulla	1.70+/−0.09	25+/−11.35	16+/−4.04	1.6+/−0.12	25+/−6.15
s2	**cortex**	2.4+/−0.17	7+/−4.14	16+/−8.07	1.9+/−0.30	11+/−2.41
	medulla	2.2+/−0.15	10+/−3.94	13+/−6.08	1.7+/−0.20	25+/−3.48
s3	**cortex**	1.4+/−0.28	13+/−6.01	22+/−6.20	1.1+/−0.67	12+/−8.43
	medulla	1.6+/−0.18	29+/−12.80	21+/−6.45	1.4+/−0.28	23+/−4.91
s4	**cortex**	1.6+/−0.20	22+/−8.28	18+/−4.30	1.2+/−0.72	9+/−6.03
	medulla	1.6+/−0.13	17+/−10.97	20+/−4.99	1.5+/−0.20	24+/−5.64
s5	**cortex**	1.90+/−0.08	12+/−3.31	18+/−3.63	1.5+/−0.74	10+/−5.56
	medulla	1.7+/−0.22	14+/−5.85	16+/−5.43	1.7+/−0.26	18+/−5.33
s6	**cortex**	1.8+/−0.18	8+/−7.66	25+/−7.55	1.6+/−0.19	16+/−3.72
	medulla	1.7+/−0.17	29+/−17.81	24+/−10.43	1.4+/−0.21	33+/−6.15
s7	**cortex**	1.7+/−0.21	7+/−6.31	23+/−10.28	1.8+/−0.28	13+/−4.92
	medulla	1.75+/−0.09	24+/−12.30	20+/−5.11	1.5+/−0.13	27+/−5.80
s8	**cortex**	1.7+/−0.15	9+/−5.65	19+/−3.69	1.8+/−0.20	16+/−4.85
	medulla	1.7+/−0.17	14+/−7.08	18+/−3.94	1.7+/−0.22	29+/−4.74
s9	**cortex**	1.6+/−0.17	15+/−8.85	16+/−6.04	1.7+/−0.19	13+/−3.70
	medulla	1.6+/−0.12	18+/−12.03	21+/−6.42	1.5+/−0.22	26+/−4.91
s10	**cortex**	2.1+/−0.28	12+/−7.59	15+/−7.19	1.7+/−0.27	15+/−4.75
	medulla	2.0+/−0.40	16+/−6.47	14+/−3.93	1.5+/−0.19	34+/−6.68
Subject average	**cortex**	1.8+/−0.27	12+/−4.39	19+/−3.12	1.6+/−0.25	13+/−2.33
	medulla	1.7+/−0.21	20+/−6.39	18+/−3.42	1.5+/−0.12	26+/−4.67

Table 2.

Precision of the parameters are compared using coefficient of variation (CV), reported as percentage and the normalized RMSE (nRMSE). Each row reports on model fitting results obtained from data before applying any correction (no correction) and after applying both distortion and motion correction (Di+MoCo). The coefficient of variation for all parameters and residuals were smallest after applying Di+MoCo.

Model param CV (%) / method		**No correction**	**Di+MoCo**
IVIM	**CV Slow diff. (D) [%]**	16.98+/−4.63	14.72+/−5.52
	CV Fast diff. (D*) [%]	58.15+/−28.19	46.91+/−9.79
	CV Perf. Frac, (f) [%]	34.62+/−15.25	30.49+/−7.34
	nRMSE	0.30+/−0.05	0.17+/−0.05
DTI	**CV MD [%]**	6.50+/−1.25	3.28+/−1.17
	CV FA [%]	14.51+/−1.67	12.09+/−2.31
	nRMSE	0.35+/−0.06	0.12+/−0.02